

# Transport Mechanisms of Small Molecules through Polyamide 12/Montmorillonite Nanocomposites

B. Alexandre,<sup>†</sup> L. Colasse,<sup>†</sup> D. Langevin,<sup>†</sup> P. Médéric,<sup>‡</sup> T. Aubry,<sup>‡</sup> C. Chappey,<sup>†</sup> and S. Marais<sup>\*,†</sup>

Université de Rouen, Laboratoire Polymères, Biopolymères, Surfaces, UMR6270 CNRS & FR 3038, 76821 Mont-Saint-Aignan Cedex, France, and Equipe Rhéologie du LIMATB EA4250, Université de Bretagne Occidentale, 6 Av. Le Gorgeu, C.S. 93837, 29238 Brest Cedex 3, France

Received: December 9, 2009; Revised Manuscript Received: March 26, 2010

The aim of this work is to study the transport of small molecules through the hybrid systems polyamide 12 (PA12)/organo-modified montmorillonite (Cloisite 30B, C30B) prepared by melt blending, using two blending conditions. The transport mechanisms were investigated by using three probe molecules: nitrogen, water, and toluene. While a barrier effect appears clearly with nitrogen, this effect changes with the amount of fillers for water and disappears for toluene. The reduction of permeability for nitrogen is mainly due to the increase of tortuosity. For water and toluene, the permeation kinetics reveals many concomitant phenomena responsible for the permeation behavior. Despite the tortuosity effect, the toluene permeability of nanocomposites increases with C30B fraction. The water and toluene molecules interact differently with fillers according to their hydrophilic/hydrophobic character. Moreover, the plasticization effect of water and toluene in the matrix, involving a concentration-dependent diffusion coefficient, is correctly described by the law  $D = D_0 e^{\gamma C}$ . On the basis of Nielsen's tortuosity concept, we suggest a new approach for relative permeability modeling, not only based on the geometrical parameters (aspect ratio, orientation, recovery) but also including phenomenological parameters deduced from structural characterization and permeation kinetics.

## 1. Introduction

The permeation of small molecules through polymer–clay nanocomposites has attracted substantial attention in the past decade.<sup>1–13</sup> Many studies reveal the barrier effect of nanoclay dispersion in a polymer matrix. The barrier effects of gas and liquid are generally attributed to the tortuosity phenomenon, corresponding to an increase of the diffusion path through the matrix. The tortuosity effect is directly related to the dispersion state of the clay nanoplatelets.<sup>14,15</sup> The dispersion state depends on the compatibility between the clay and the polymer matrix. The inorganic clay surface is often modified by chemical treatments to improve the affinity of clay toward the polymeric matrix, and the type of organic treatment is known to influence the degree of dispersion of the clay in the matrix.<sup>16–18</sup> In addition, the dispersion state also depends on the organoclay content:<sup>19</sup> for nanocomposites, it generally decreases with increasing organoclay content.<sup>20</sup> The techniques and methods used to prepare the hybrid materials are also very important in terms of the structural organization of the clay nanoplatelets in the polymer matrix. For nanocomposites constituted of a polyurethane matrix highly filled with different Cloisite series, Herrera-Alonso et al.<sup>21</sup> have shown that preprocessing clay samples with sonication leads to an improvement of barrier properties, explained by the high aspect ratio of clay entities (~100). Regarding blending methods, the design of the mixing device and the melt processing conditions, i.e., temperature, blade rotation speed, and residence time,<sup>22,23</sup> play a key role in achieving the structure and properties of the final product.<sup>24</sup>

Nevertheless, the optimization of these parameters is not sufficient to allow clay particles to be completely exfoliated.<sup>25</sup> The total exfoliation of the clay particles is rather difficult to obtain by melt blending methods, so most polymer–clay nanocomposites exhibit a partially intercalated/exfoliated structure. Most studies on polymer nanocomposite barrier properties are based on the tortuous pathway concept,<sup>14</sup> for which the nanofiller phase is assumed to be impermeable for gas and liquid molecules. The very few models developed on the tortuosity concept take into account only the volume fraction of fillers, the aspect ratio, and the orientation of nanoclays.<sup>11,26</sup> From a general point of view, a purely geometrical approach is not adequate to describe correctly and then model the permeation properties of nanocomposites, in particular when interactions exist between diffusing molecules and the components of the composites, such as the polymeric matrix, which can be plasticized by vapor molecules; in that case, a dependence of the diffusion coefficient on the permeant concentration should be included in the modeling. Moreover, in the geometrical approach, the role played by the clay/matrix interface is usually neglected. The possible variation of the crystalline phase of the matrix, due to the presence of nanoclays, is also neglected in the geometrical models. Recently, Picard et al.<sup>7</sup> have highlighted the interest of (i) considering the variation of the crystalline phase of the matrix, the polydispersity of the montmorillonite structure, and (ii) taking into account the presence of surfactant at the clay surface to model the nanocomposite transport properties appropriately.

The aim of the present work was to study the effect of the filler loading on the barrier performance of polyamide 12 (PA12)/montmorillonite composites and to give a new physical insight into the permeation properties from the detailed analysis of the permeation kinetics and structure properties. More

\* Corresponding author. Tel.: +33-235146702. Fax: +33-235146704. E-mail: stephane.marais@univ-rouen.fr.

<sup>†</sup> Université de Rouen.

<sup>‡</sup> Université de Bretagne Occidentale.

**TABLE 1: Comparison between Theoretical Clay Mass Fraction and Clay Mass Fraction Measured by TGA, Converted into Volume Fraction of Impermeable Fillers (Free Ammonium Cation Modifier) of PA12/C30B Nanocomposites**

|                                  | theoretical<br>clay mass<br>fraction,<br>denoted $x$ ,<br>(%) | measured<br>clay mass<br>fraction<br>(%) | $\phi_v$ volume<br>fraction<br>(%) | $\phi_i$ volume<br>fraction of<br>impermeable<br>filler (%) |
|----------------------------------|---|--|------------------------------------|---|
| PA12/C30B                        | 1.5   | 1.63–1.66                                | 0.84–0.85                          | 0.43–0.43   |
| $N_{32}^{5\%}$ – $N_{100}^{5\%}$ | 3   | 2.63–2.27                                | 1.36–1.17                          | 0.69–0.61   |
|                                  | 5   | 4.70–5.42                                | 2.45–2.84                          | 1.27–1.47   |
|                                  | 8   | 8.07–8.13                                | 4.29–4.32                          | 2.20–2.23   |
|                                  | 10  | 9.36–9.05                                | 5.00–4.83                          | 2.61–2.49   |

precisely, the barrier properties of PA12/montmorillonite systems were investigated not only by considering the effect of the dispersion state of clay platelets and the structure of the matrix but also by taking into account: (1) the interactions between the diffusing species and the components of the nanocomposite and (2) the physicochemical properties of the clay/matrix interface, playing on the hydrophobic or hydrophilic character of the permeant. To achieve this objective, the transport properties of these hybrid materials have been performed with diffusing molecules, differing in their kinetic diameter and their interaction capacity: nitrogen for its chemical inertia (very few interactions with matrix and clay) and water (polar molecule) and toluene (apolar molecule) for their ability to interact differently with the matrix and the montmorillonite. To model the permeation behavior, a quantitative description of the montmorillonite particle dispersion has been carried out. Moreover, the diffusion mechanism approach, based on a concentration-dependent diffusion coefficient in the case of water,<sup>27</sup> is used for the analysis of the toluene permeation kinetics in the present paper.

## 2. Experimental Section

**2.1. Materials.** The matrix used in this study was a commercial polyamide 12 (PA12), referenced as Rilsan AECHVO from ARKEMA (Serquigny, France). Its mass and number average molecular mass are equal to 37 000 and 20 000 g/mol, respectively, and the melting point of PA12 is 178 °C.<sup>27</sup> The organo-modified montmorillonite Cloisite 30B (C30B), bearing a (tallow alkyl) methyl bis(2-hydroxyethyl) ammonium cation was supplied by Southern Clay Products (Gonzales, Texas). The tallow alkyl chains have the following composition: ~65% C18; ~30% C16; ~5% C14. The specific gravity of C30B is equal to 2 g/cm<sup>3</sup>, and the amount of ammonium cations of C30B is estimated by TGA to be ~25 wt %.

**2.2. Preparation of Composite Films.** PA12/C30B nanocomposites, for C30B mass fraction ranging from 1.5 to 10% (0.8 to 5% in volume fraction, see Table 1), were prepared by melt intercalation in a Haake Rheocord internal mixer. All the composites were mixed for 6 min, at a temperature of 200 °C at which PA12 and clays are thermally stable.<sup>27,28</sup> Two rotation blade speeds were used: 32 and 100 rpm. Composite films were obtained by compression molding at 200 °C to obtain 200–250  $\mu$ m thick plates. For the sake of clarity, the composite films were named  $N_y^{x\%}$ , where  $x$  represents the volume fraction of montmorillonite and  $y$  the rotation blade speed (e.g.,  $N_{32}^{5\%}$  is a nanocomposite containing 5% volume fraction of C30B and prepared with a rotation speed of 32 rpm).

**2.3. Film Characterization.** The mass fraction of montmorillonite and the temperature marking the onset of degradation

of composite films were determined by thermal gravimetric analysis. The experiments were performed with a TGA device (TGA-7 Perkin-Elmer) from 40 to 700 °C at 10 °C/min under a nitrogen atmosphere.

Clay dispersion was investigated by two techniques: (1) wide-angle X-ray diffraction, WAXD, to get the clay  $d$ -spacing,  $d_{001}$ , and (2) transmission electron microscopy, TEM, to obtain information on the state of dispersion of the clay particles.

**XRD Experiments.** Wide-angle X-ray diffraction was carried out with an X-ray diffraction D8 Advance diffractometer from Bruker AXS. The source wavelength was  $\lambda = 1.79$  Å, corresponding to the  $\alpha$  line of Co. The sample was placed in a Bragg–Brentano configuration. The  $2\theta$  diffraction diagrams were determined between 2° and 15°. The samples were studied under the same experimental conditions and held on a silicon substrate that did not exhibit any diffraction line in the diffraction angle range considered. The  $d$ -spacing was estimated from (001) peaks in the WAXD patterns with Bragg's formula.

**TEM Experiments.** For transmission electron microscopy observations, the films were embedded directly in Spurr resin before cutting at room temperature on an Ultracut UCT microtome (Leica-Vienne). Ultrathin sections were collected on Formvar carbon-coated 100-mesh nickel grids and directly observed in TEM. The TEM observations were performed on a Tecnai 12 Biotwin microscope (FEI Company-Eindhoven) operating at 80 kV. Images were acquired with a CCD Megaview II camera controlled by Analysis software (Eloise, France).

The polymer crystalline structure and degree of crystallinity were studied by wide-angle X-ray diffraction experiments and by differential scanning calorimetry (DSC), respectively. The previously described WAXD experiments were extended to the  $2\theta$  range from 15° to 35° to study the matrix crystalline structure.

**DSC Experiments.** DSC data were obtained by using the conventional differential scanning calorimeter Perkin-Elmer DSC-7. Samples with a mass of about 12 mg were heated under nitrogen atmosphere to minimize the oxidative degradation. The heating step was carried out from 50 to 200 °C at a rate of 10 °C/min. Before all DSC experiments, the baseline was calibrated using empty aluminum pans, and the DSC apparatus was calibrated using melting temperature and enthalpy of a high-purity indium standard (156.6 °C and 28.45 J/g). The degree of crystallinity ( $X_c$ ) was determined by

$$X_c = \frac{\Delta H_m}{(1 - \phi)\Delta H_m^0} \times 100 \quad (1)$$

where  $\Delta H_m$  is the apparent melting enthalpy;  $\Delta H_m^0$  is the extrapolated value of the enthalpy corresponding to the melting of 100% crystalline PA12 ( $\Delta H_m^0 = 245$  J/g<sup>29</sup>); and  $\phi$  is the mass fraction of montmorillonite determined by TGA experiments.

**Permeation Experiments.** The permeation properties of nanocomposites were studied with methods appropriate to the nature of the diffusing molecules. Before each analysis, samples were dried in desiccators under vacuum pressure with P<sub>2</sub>O<sub>5</sub>. All permeation measurements were performed at 25 °C.

The nitrogen permeation measurements were carried out by the “time-lag” method, a variable pressure method.<sup>30</sup> The gas permeation cell consisted of two compartments separated by the film studied. A preliminary high vacuum desorption was realized on both sides of the film lasting at least 48 h. Then, the upstream side was provided with nitrogen under test at

pressure  $p_1 = 3$  bar. The increased pressure in the downstream compartment ( $p_2$ ) was recorded as a function of time with a datametric pressure sensor (PFEIFFER VACUUM, 0–1 mBar). A steady state line was obtained after a transitory state. The permeability coefficient,  $P$ , expressed in barrer units (1 barrer =  $10^{-10}$  cm<sup>3</sup>(STP) cm cm<sup>-2</sup> s<sup>-1</sup> cmHg<sup>-1</sup>) was calculated from the slope of the steady state line ( $dp/dt$ )

$$P = \frac{dp}{dt} \frac{LV}{RT\Delta p} \quad (2)$$

where  $\Delta p$  is the pressure difference between the two faces of the film;  $A$  is the exposed area (3.087 cm<sup>2</sup>);  $L$  is the thickness of the film;  $R$  is the ideal gas constant; and  $V$  is the downstream volume (70.3 cm<sup>3</sup>).  $T$  is the experiment temperature (298 K).

The water and toluene vapor permeation measurements were carried out by using a pervaporation method,<sup>31</sup> which consists of measuring the permeation flux through the film, as a function of time, at different permeant concentrations. This differential permeation method allows the diffusion and permeability coefficients of the film to be determined.

For water, the permeation cell consists of two compartments separated by the film. First, dry nitrogen was flushed into both compartments over many hours to dry the film. In a second step, a stream of liquid water was pumped through the upstream compartment. Then, the water concentration in the initially dry nitrogen sweeping gas was monitored in the downstream compartment via the hygrometric sensor (mirror hygrometer from General Eastern Instruments) and a data acquisition system. The flux  $J(L, t)$  at the dry interface is given by

$$J(L, t) = \frac{Q(x^{\text{out}} - x^{\text{in}})}{A RT} p_t \quad (3)$$

where  $A = 30$  cm<sup>2</sup> is the film surface area;  $Q = 9.3$  cm<sup>3</sup> s<sup>-1</sup> is the flow rate of the carrier gas sweeping the downstream face;  $T$  is the experiment temperature (298 K); and  $(x^{\text{out}} - x^{\text{in}})$  is the water concentration expressed in ppmV and determined at the outlet and inlet of the permeation cell.<sup>32,33</sup>

For toluene, the permeation measurement device was similar to that used for water.<sup>31</sup> The film was mounted in the cell, and then toluene was introduced in the upstream compartment. Toluene concentration in the nitrogen sweeping gas, initially free of toluene, was monitored in the downstream compartment via a Flame Ionization Detector (FID) (VARIAN CP-3380). The flux  $J(L, t)$  was determined from eq 3, with  $A = 13.75$  cm<sup>2</sup> and  $Q = 0.5$  cm<sup>3</sup> s<sup>-1</sup>, and  $x^{\text{out}} - x^{\text{in}}$  is the toluene concentration measured by FID. For water and toluene, the permeability coefficient was obtained from the steady state flux by

$$P = \frac{J_{\text{st}} L}{\Delta a} \quad (4)$$

where  $J_{\text{st}}$  is the stationary flux;  $\Delta a$ , practically equal to 1, is the difference in water or toluene activity between the two faces of the film; and  $P$  is expressed in barrer units.

### 3. Modeling of Transport Mechanisms

**3.1. Relative Permeability for Gas (Geometrical Approach).** The nitrogen relative permeability, corresponding to the ratio between permeability of composite  $P_c$  and permeability

of matrix  $P_m$ , was modeled by the geometrical path model proposed by Bharadwaj<sup>15</sup>

$$\frac{P_c}{P_m} = \frac{1 - \phi_i}{1 + \frac{\alpha}{2} \phi_i \left( \frac{2}{3} \right) \left( O + \frac{1}{2} \right)} \quad (5)$$

The key parameters of this model are the volume fraction of the impermeable fillers,  $\phi_i$  (volume fraction of montmorillonite without ammonium cation), reported in Table 1, the particle aspect ratio,  $\alpha$ , and the orientation parameter of the clay platelets,  $O$ . For  $O = 1$ , eq 5 leads to Nielsen's formula, corresponding to particles perpendicularly oriented to the diffusion flux.<sup>14</sup> Random particle orientation corresponds to  $O = 0$ .

**3.2. Relative Permeability for Water and Toluene.** The Nielsen and Bharadwaj models,<sup>14,15</sup> previously used for modeling the nitrogen relative permeability, as well as the other models reported in the literature based on a geometrical approach,<sup>11,34,35</sup> are inappropriate for the vapor relative permeability of nanocomposites studied in this work. Indeed, the diffusion coefficient is generally assumed constant for gas permeation, while for liquid or vapor permeation, a variation of the diffusion coefficient during the permeation process can be observed. For the polyamide aliphatic polymer, the diffusion coefficient increases exponentially with the local permeant concentration in the film during the course of water or toluene penetration.<sup>33,36</sup> This diffusion-concentration dependence was generally attributed to a plasticization effect of the material by the penetrant leading to an increase of the free volume<sup>37</sup> and generally described by the exponential law<sup>38,39</sup>

$$D = D_0 e^{\gamma C} \quad (6)$$

where  $D_0$  is the limit diffusion coefficient;  $\gamma$  is the plasticization coefficient; and  $C$  is the local permeant concentration. The minimum free volume necessary to disperse diffusing molecules into the polymer is not negligible compared to the mean free volume, so the chain segments reorganize themselves to enable the penetrant to jump from one cavity to another. According to Frisch,<sup>40</sup> this corresponds to a Fickian type B mechanism, which is generally observed with organic vapors and can be characterized by (1) a nondiluted polymer–penetrant system, (2) a concentration-dependent diffusion coefficient, and (3) a dependence of activation energies on temperature.

To determine both parameters of this law, we use a method which is described in more detail in a separate paper.<sup>41</sup> During the fitting procedure of the experimental transient flux data,  $D_M$  (the maximum value of  $D$  for  $C = C_{\text{eq}}$ ,  $D_M = D_0 e^{\gamma C_{\text{eq}}}$ ),  $D_0$ ,  $\gamma$ ,  $C_{\text{eq}}$ , and  $\langle D \rangle$  are computed.  $C_{\text{eq}}$  is the penetrant concentration in the polymer at sorption equilibrium, and  $\langle D \rangle$  is the mean integral diffusion coefficient characterizing the average diffusion coefficient of the penetrant in the materials.<sup>36</sup>

For the relative permeability, the permeability is usually considered as the product of the diffusivity, supposed constant, and the solubility.

In this case, it is more convenient to consider

$$P = \langle D \rangle S \quad (7)$$

with  $S$  being the solubility coefficient and  $\langle D \rangle$  the mean integral diffusion coefficient that becomes, using the concentration dependence law of  $D$  (eq 6)



$$\langle D \rangle = \frac{D_0(e^{\gamma C_{eq}} - 1)}{\gamma C_{eq}} \quad (8)$$

Then, the water relative permeability can be calculated from eq 7

$$\frac{P_c}{P_m} = \frac{\langle D \rangle_c C_{eq_c}}{\langle D \rangle_m C_{eq_m}} \quad (9)$$

The index m stands for matrix, and the index c stands for composite.

## 4. Results and Discussion

**4.1. Dispersion and Structure of PA12/Montmorillonite Systems.** The mass fraction of montmorillonite in the composite films was determined by thermogravimetric analysis. The amount of montmorillonite was obtained from total matrix degradation, subtracting the mass losses due to moisture desorption. The mass fraction of montmorillonite is reported in Table 1. For the PA12/C30B systems studied, the mass fraction is close to the theoretical mass fraction introduced during the compound preparation and reveals a rather good homogeneity of dispersion on a microscopic scale, for all compounding conditions tested.

The structure of all composites was investigated by WAXD and TEM. In Figure 1, the C30B powder diffractogram is compared to those of all nanocomposites. The (001) basal-plane spacing ( $d_{001}$ ) of C30B is 1.8 nm. For the PA12/C30B films, N<sub>32</sub><sup>%</sup> and N<sub>100</sub><sup>%</sup>, the position of the diffraction peak of C30B is shifted to a lower  $2\theta$  angle compared to that of the original C30B. The interlayer distance of C30B, calculated from WAXD reflections, is 3.2 nm, highlighting the intercalation of PA12 chains into the C30B galleries. Micrographs of N<sub>32</sub><sup>%</sup> and N<sub>100</sub><sup>%</sup> nanocomposites show isolated clay layers and small stacks of clay layers, for low C30B volume fractions,  $\phi \leq 2.5\%$  (Figure 2). For high C30B fractions ( $\phi \geq 2.5\%$ ), the presence of a few clay aggregates is evidenced in Figure 2. In fact, WAXD and TEM analyses show a complex structure where intercalated and exfoliated structures coexist for both systems.

However, a previous study performed by Médéric et al.<sup>42</sup> pointed out slightly different structures depending on the blade rotation speed: nanocomposites prepared at 100 rpm exhibited a better exfoliation degree than nanocomposites processed at 32 rpm. Using the concept of specific particle density (dp) defined by Fornes et al.,<sup>43</sup> a statistical analysis based on TEM micrographs was performed over a large number of particles for each nanocomposite studied. Table 2 gives the specific particle density, dp, that is, the average number of particles per square micrometer divided by the clay mass fraction. dp decreases with increasing C30B volume fraction, and except for N<sub>100</sub><sup>0.8%</sup>, an increase of dp with increasing blade rotation speed is observed. Nanocomposites processed at 100 rpm exhibit a better exfoliation degree, compared to nanocomposites prepared at 32 rpm, leading to an improvement of rheological<sup>42</sup> and mechanical properties.<sup>27,44</sup>

Another important physical property influenced by the composite structure is the thermal stability: exfoliated systems present a better stability than intercalated ones.<sup>44</sup> The temperature marking the onset of degradation ( $T_{onset}$ ) was calculated from TGA curves by extrapolating the curve at the peak of degradation back to the initial mass of the polymer.  $T_{onset}$  of the PA12 matrix and all the composites studied in the present

work is reported in Table 3. The presence of montmorillonite is shown to increase  $T_{onset}$  systematically. For the same montmorillonite content,  $T_{onset}$  of N<sub>100</sub><sup>%</sup> nanocomposites is found to be higher than that for N<sub>32</sub><sup>%</sup> nanocomposites. This result confirms that N<sub>100</sub><sup>%</sup> are better exfoliated systems than N<sub>32</sub><sup>%</sup> systems.

### 4.2. Crystalline Structure and Crystallinity of Polyamide

**12.** Crystalline lamellae are considered to be impermeable to small molecules. It is thus necessary to take into account any crystalline changes in the polymer matrix, in the presence of clay, that could modify the permeation properties. The crystalline structure of composites was investigated by WAXD. Figure 3 shows the diffraction patterns of N<sub>32</sub><sup>%</sup> and N<sub>100</sub><sup>%</sup> nanocomposites. The same diffraction peak at  $2\theta \sim 25^\circ$ , corresponding to the Miller index (001) of the pseudohexagonal  $\gamma$  form of the PA12 matrix, is observed for each nanocomposite. The crystalline structure of the PA12 matrix does not seem to be affected by the presence of C30B. The degree of crystallinity,  $X_c$ , was given from the melting and crystallization enthalpies obtained by DSC thermograms. The  $X_c$  data are reported in Table 4, showing that the degree of crystallinity in PA12 is practically unchanged by the presence of C30B.

As a conclusion, the crystallinity index of PA12 can be considered as independent of clay content. As a consequence, the possible changes of transport properties induced by clay will not be attributed to changes in the crystallinity of the polymer matrix.

### 4.3. Transport Properties. 4.3.1. Nitrogen Permeability.

It is well-known that gas molecules, except for CO<sub>2</sub>, have no, or at least very few, interactions with polymeric materials, leading to a linear Henry's sorption law and to a constant diffusion coefficient, especially in the case of rubbery polymers. In the case of glassy polymers, a dual-mode sorption can exist that combines gas sorption in the amorphous regions of the polymer (Henry's law) with gas trapped in polymer microvoids, analogous to the adherence of gas molecules to sites on the surface of porous adsorbents (Langmuir equation) leading to a sigmoidal variation of D.<sup>45</sup> The nitrogen molecule was used to study the influence of the partially intercalated/exfoliated structure of clay on the transport properties of PA12/montmorillonite films. The nitrogen permeability coefficients of all the composites studied are reported in Table 5. In accordance with the tortuosity concept, the nitrogen permeability decreases with the presence of C30B nanoparticles in the PA12 matrix. For all nanocomposites, the barrier effect increases with the amount of C30B content. However, the difference in structure between N<sub>32</sub><sup>%</sup> and N<sub>100</sub><sup>%</sup> series seems to affect the barrier properties slightly. To examine more precisely the barrier properties, the nitrogen relative permeability, corresponding to the ratio between permeability of composite  $P_c$  and permeability of matrix  $P_m$ , was plotted (eq 5) versus C30B volume fraction in Figure 4.

The aspect ratio was measured from TEM micrographs,  $\alpha_{mes} \sim 15$ .<sup>27</sup> It is well-known that the difficulty in determining the aspect ratio from TEM micrographs, due to the curvature, orientation, recovery, and flexibility of clay platelets, leads to the underestimation of the  $\alpha_{mes}$  value. Experimental data of relative permeability were fitted by eq 5 from the root-sum-square (RSS) method. In the case of oriented particles ( $O = 1$ ), Nielsen's formula leads to  $\alpha = 68$  and  $\alpha = 78$ , for N<sub>32</sub><sup>%</sup> and N<sub>100</sub><sup>%</sup> nanocomposites, respectively. Considering random particle orientation ( $O = 0$ ), the best fitting of experimental data was obtained with  $\alpha = 200$  for N<sub>32</sub><sup>%</sup> and  $\alpha = 233$  for N<sub>100</sub><sup>%</sup>. It is interesting to note that the apparent aspect ratio of primary clay entities, determined from intrinsic viscosity,<sup>42</sup> has the same order of magnitude,  $\alpha = 220$  for N<sub>32</sub><sup>%</sup> and  $\alpha = 280$  for N<sub>100</sub><sup>%</sup>. The

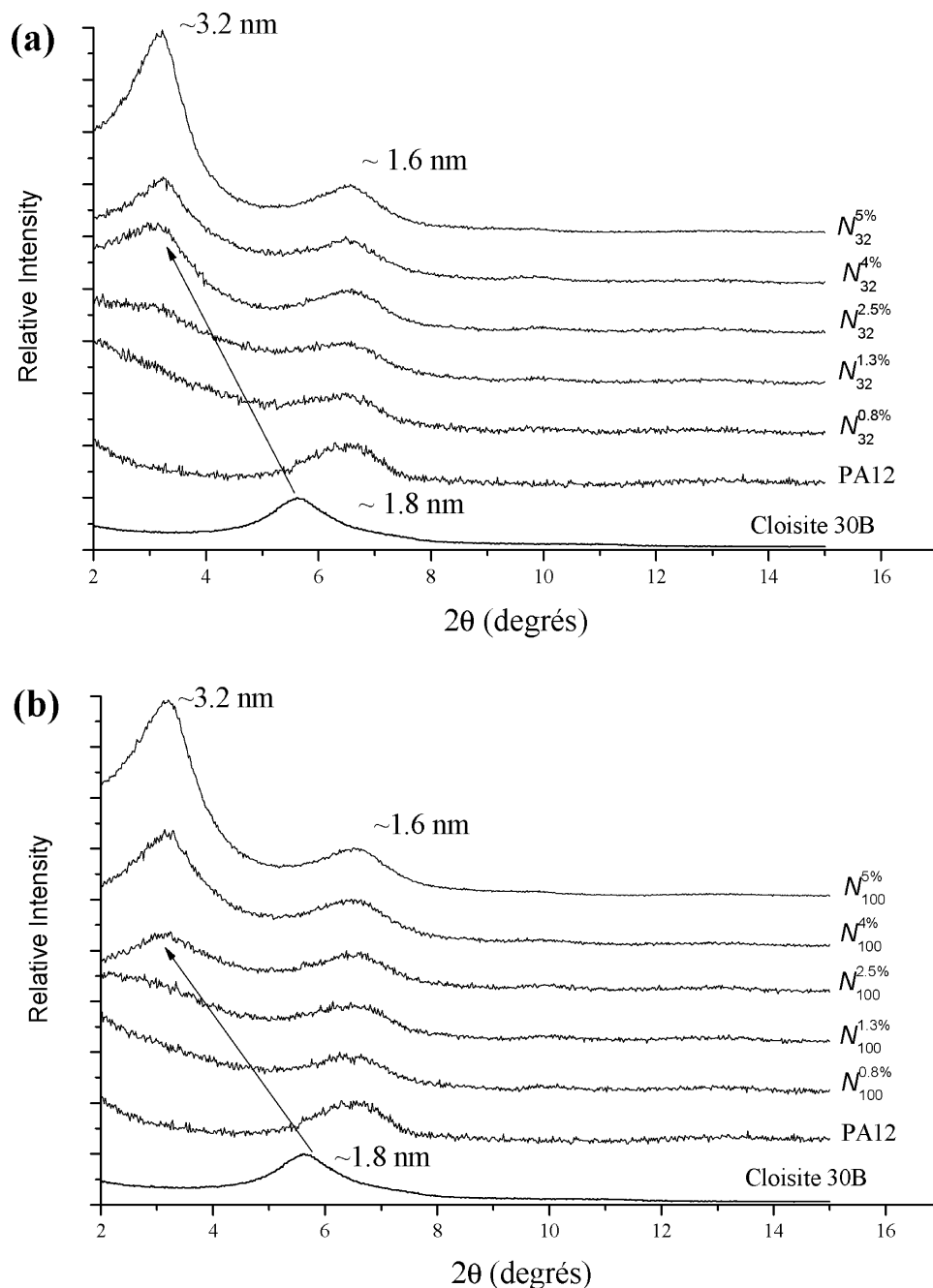


**Figure 1.** X-ray diffractograms of (a)  $N_{32}^{5\%}$  and (b)  $N_{100}^{5\%}$  nanocomposites.

modeling approach shows that C30B entities can be considered as high aspect ratio particles, even if aspect ratio values superior to 200 are certainly too high because (i) clay exfoliation is not completely achieved, as shown by XRD and TEM results, and (ii) mean orientation parameter  $O$  should be taken between 0 (random) and 1 (oriented). Anyway, fitting of permeability data and rheology data confirms that the exfoliation degree of the  $N_{100}^{5\%}$  nanocomposite is higher than that of the  $N_{32}^{5\%}$  nanocomposite.

On the other hand, these geometrical models neglect the possible physical modifications of the crystalline phase of the matrix and the role played by the clay/matrix interface on the mobility of the amorphous phase of the matrix near this interface. Xu et al.<sup>46</sup> have developed a chain-segment immobility factor and shown that the chain confinement could enhance the barrier properties of intercalated nanocomposites. Nevertheless, from the experimental point of view, it is rather difficult to highlight clearly the role played by the chain-segment mobility

in nanocomposites. Moreover, it is not easy to determine the immobility factor. In conclusion, tortuosity might not be due solely to the obstruction diffusion of nitrogen by nanoplatelets but also to the reduction of chain-segment mobility around the filler.

**4.3.2. Water Permeability.** Unlike nitrogen molecules, the water molecules can interact with the PA12 matrix and the clay–matrix interfaces. Contrary to the nitrogen permeation property, the water permeability does not decrease systematically in the presence of montmorillonite (Table 5). More precisely, the water permeability of nanocomposites tends to decrease with the clay fraction, at the low C30B volume fractions for mixing conditions used in this work (Figure 5), but beyond 2.5% for  $N_{32}^{5\%}$  and 4% clay for  $N_{100}^{5\%}$ , an increase of the water relative permeability can be observed, in particular for  $N_{32}^{5\%}$ . At low C30B volume fractions, the decrease of water permeation is mostly due to the tortuosity effect and possibly to the reduction of chain

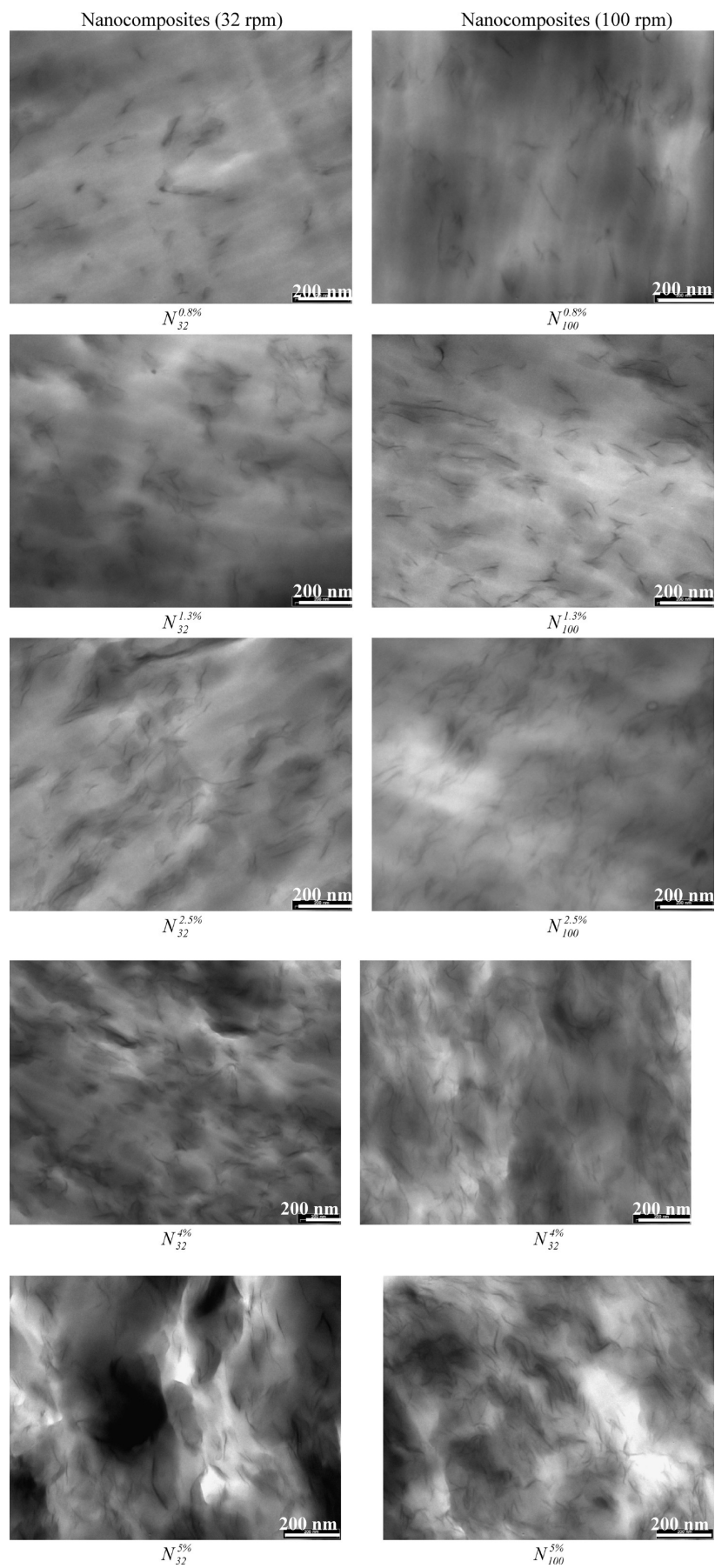


**Figure 2.** TEM micrographs of  $N_{32}^{x\%}$  and  $N_{100}^{x\%}$  nanocomposites, for different C30B fractions (scale 200 nm).

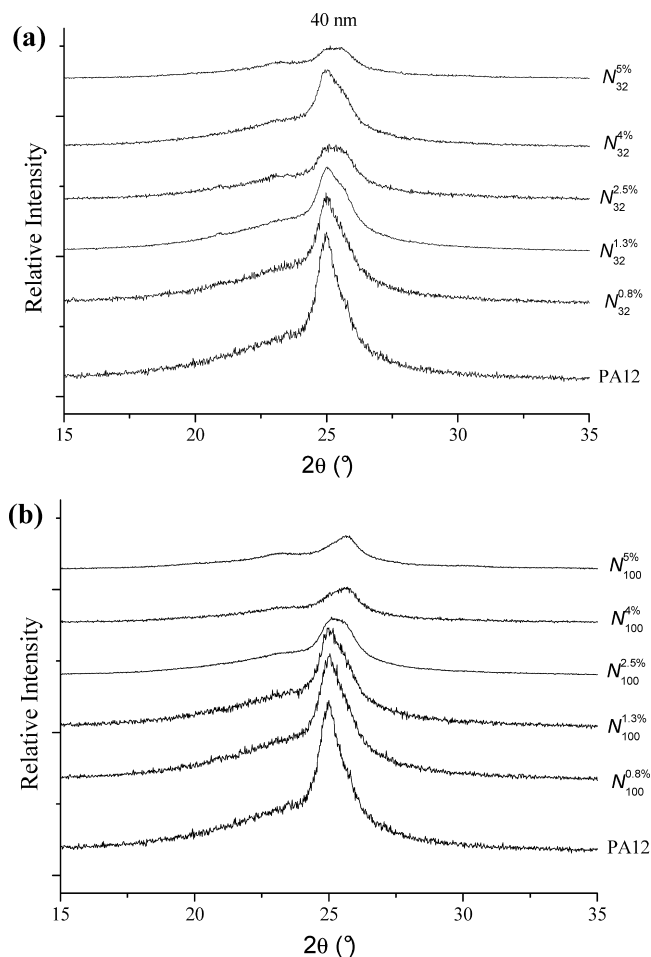
**TABLE 2: Specific Particle Density  $\rho_p$ , i.e., Average Number of Particles per Square Micrometer Divided by the Clay Mass Fraction, for the Nanocomposites Prepared at Two Blade Rotation Speeds**

| nanocomposites                   | $\rho_p$ |
|----------------------------------|----------|
| $N_{32}^{0.8\%}-N_{100}^{0.8\%}$ | 53–39    |
| $N_{32}^{1.3\%}-N_{100}^{1.3\%}$ | 54–64    |
| $N_{32}^{1.5\%}-N_{100}^{1.5\%}$ | 27–31    |
| $N_{32}^{4\%}-N_{100}^{4\%}$     | 28–30    |
| $N_{32}^{5\%}-N_{100}^{5\%}$     | 23–32    |

**TABLE 3: Degradation Temperature,  $T_{\text{onset}}$ , of PA12 and PA12/C30B Nanocomposites**

|                                  | $T_{\text{onset}}$ (°C) |
|----------------------------------|-------------------------|
| PA12                             | 460                     |
| $N_{32}^{0.8\%}-N_{100}^{0.8\%}$ | 472–489                 |
| $N_{32}^{1.3\%}-N_{100}^{1.3\%}$ | 489–494                 |
| $N_{32}^{2.5\%}-N_{100}^{2.5\%}$ | 480–482                 |
| $N_{32}^{4\%}-N_{100}^{4\%}$     | 484–488                 |
| $N_{32}^{5\%}-N_{100}^{5\%}$     | 480–486                 |

mobility in the amorphous phase located around the clays. So, for the weakly filled nanocomposites, the Nielsen and Bharadwaj model (eq 5) correctly predicts the decrease of relative permeability (Figure 5). At higher C30B volume fractions, the percolation effect and water sorption, especially for the less exfoliated nanocomposite, counterbalanced the tortuosity effect, explaining the increase of water permeation.

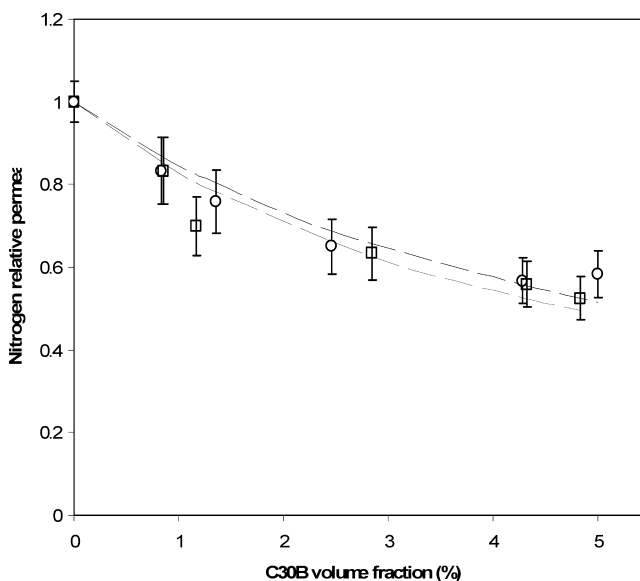
**Figure 3.** X-ray crystalline structure of (a)  $N_{32}^x\%$  and (b)  $N_{100}^x\%$  nanocomposites.**TABLE 4: Crystallinity of Matrix PA12 and PA12/C30B Nanocomposites**

|                                  | $X_c$ (%) |
|----------------------------------|-----------|
| PA12                             | 18.5      |
| $N_{32}^{0.8\%}-N_{100}^{0.8\%}$ | 16.9–18.3 |
| $N_{32}^{1.3\%}-N_{100}^{1.3\%}$ | 17.3–17.9 |
| $N_{32}^{2.5\%}-N_{100}^{2.5\%}$ | 17.6–18.3 |
| $N_{32}^{4\%}-N_{100}^{4\%}$     | 16.5–17.0 |
| $N_{32}^{5\%}-N_{100}^{5\%}$     | 16.3–17.8 |

**TABLE 5: Permeability Values of Nitrogen, Water, and Toluene, for PA12 and PA12/C30B Nanocomposites**

| films                            | $P_{N_2}$ (barrier <sup>a</sup> ) | $P_{H_2O}$ (barrier) | $P_{\text{toluene}}$ (barrier) |
|----------------------------------|-----------------------------------|----------------------|--------------------------------|
| PA12                             | 0.12                              | 243                  | 5.9                            |
| $N_{32}^{0.8\%}-N_{100}^{0.8\%}$ | 0.10–0.10                         | 208–212              | 10.6–0                         |
| $N_{32}^{1.3\%}-N_{100}^{1.3\%}$ | 0.091–0.084                       | 194–179              | 13.3–59                        |
| $N_{32}^{2.5\%}-N_{100}^{2.5\%}$ | 0.078–0.076                       | 156–152              | 84–90                          |
| $N_{32}^{4\%}-N_{100}^{4\%}$     | 0.068–0.067                       | 207–145              | 43–76                          |
| $N_{32}^{5\%}-N_{100}^{5\%}$     | 0.070–0.063                       | 232–159              | 96–85                          |

<sup>a</sup> 1 barrier =  $10^{-10}$  cm<sup>3</sup> (STP) cm cm<sup>-2</sup> s<sup>-1</sup> cmHg<sup>-1</sup>.

**Figure 4.** Nitrogen relative permeability as a function of C30B volume fraction: (○) experimental results and (black — —) prediction of the tortuous path model (eq 5) for  $N_{32}^x\%$  nanocomposites with the calculated value of  $\alpha = 200$  (eq 5, with  $O = 0$ ) and  $\alpha = 68$  (eq 5, with  $O = 1$ ); (□) experimental results and (gray — —) prediction of the tortuous path model (eq 5) for  $N_{100}^x\%$  nanocomposites with the calculated value of  $\alpha = 233$  (eq 5, with  $O = 0$ ) and  $\alpha = 78$  (eq 5, with  $O = 1$ ).

To better understand this permeation behavior, the water permeation kinetics were analyzed.<sup>27</sup> On the basis of a water concentration-dependent diffusion coefficient, an excellent agreement between the experimental and calculated flux (eq 6) was obtained for all the composites tested. The influence of the montmorillonite and the role played by the clay/polymer interface on the water plasticization effect of the PA12 matrix was then examined from the parameters of the concentration-dependence law (Table 6).<sup>41,47</sup>

As far as nanocomposites are concerned, below 2.5% and 4% volume fraction of C30B for  $N_{32}^x\%$  and  $N_{100}^x\%$ , respectively, the decrease of  $D_0$  is in accordance with the tortuous path model. For highly filled nanocomposites, an increase of  $D_0$ , especially for  $N_{32}^x\%$  (the less exfoliated systems), can be observed (Table 6), which could be due to an increase of the number of hydrophilic sites with the increase of C30B content. Moreover,



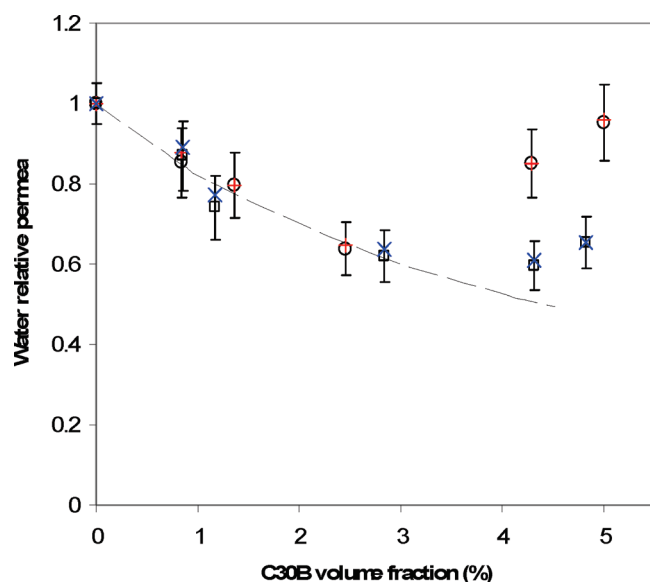


**Figure 5.** Water relative permeability as a function of C30B volume fraction: (○) experimental results and (+) calculated values (eq 9) for  $N_{32}^x\%$  nanocomposites; (□) experimental results and (×) calculated values (eq 9) for  $N_{100}^x\%$  nanocomposites, respectively; (— — —) prediction of the tortuous path model (eq 5, with  $O = 0$ ) for nanocomposites with the calculated value of  $\alpha = 233$ .

the decrease in the degree of exfoliation (cf. Table 2), due to the presence of some C30B aggregates at high volume fractions (cf. Figure 2), can facilitate the diffusion of water molecules along a new pathway, consisting of a percolation path through the clay–polymer interface zones;<sup>27</sup> this effect will be called the percolation effect in the text.

Up to 4% volume fraction of C30B,  $\gamma C_{eq}$  depends weakly on the C30B content. Nevertheless, a slight difference appears between  $N_{32}^x\%$  and  $N_{100}^x\%$  nanocomposites: the plasticization effect was found to be higher for the less exfoliated systems ( $N_{32}^x\%$ ). Above 2.5% and 4% clay, for  $N_{32}^x\%$  and  $N_{100}^x\%$ , respectively, the strong decrease of  $\gamma C_{eq}$  was explained partly by a reduction in the mobility of the polymer chain segments due to the presence of numerous dispersed clay nanoparticles.

To give more precise insight into the plasticization phenomena, the plasticization coefficient  $\gamma$  and the equilibrium water concentration  $C_{eq}$  were deduced and gathered in Table 6. For  $N_{32}^x\%$  nanocomposites, up to 2.5% clay, the increase of  $\gamma$ , revealing an increase of the free volume within the material due to the insertion of water molecules, was attributed to the greater amount of pre-existing holes resulting from the increase in the stiffness of the nanocomposite with increasing C30B content.<sup>27</sup> For  $N_{100}^x\%$  nanocomposite systems, except for 5% clay volume fraction,  $\gamma$  remains practically unchanged. This effect seems to indicate that the volume occupied by the water molecules is located preferentially in the vicinity of the C30B/PA12 interface. Moreover, this tendency can be correlated to

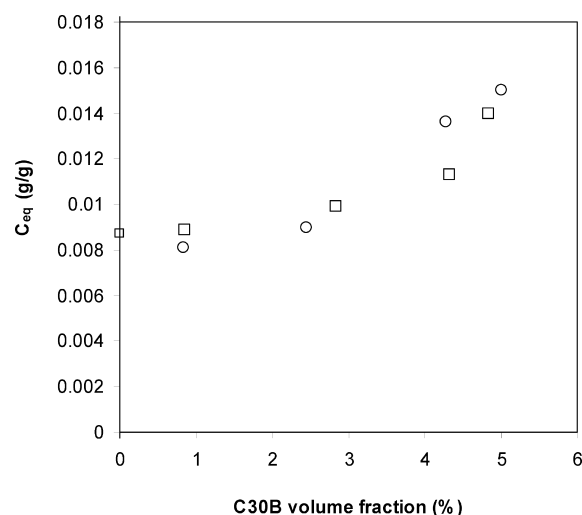


**Figure 6.** Water concentration in nanocomposites as a function of C30B volume fraction: (○) for  $N_{32}^x\%$  nanocomposites and (□) for  $N_{100}^x\%$  nanocomposites.

the better dispersion and exfoliation of C30B in  $N_{100}^x\%$  nanocomposites, leading to a reduction of the water cluster size.<sup>27,48</sup> Above 2.5% for  $N_{32}^x\%$  and 4% C30B for  $N_{100}^x\%$ , the strong drop in  $\gamma$  could result from the decrease of the free volume due to the increase in the stiffness of PA12, from the high quantity of water molecules sorbed on the great number of hydrophilic sites of C30B nanoparticles and from hydrogen bond interactions between the PA12 matrix and water molecules. For  $N_{32}^x\%$  and  $N_{100}^x\%$  nanocomposites, at clay volume fractions <4%, the equilibrium water concentration  $C_{eq}$  is of the same order of magnitude as the  $C_{eq}$  value of the PA12 matrix and remains practically constant, irrespective of the mixing conditions. Beyond 4% C30B, the increase of  $C_{eq}$ , especially marked for the  $N_{32}^x\%$  nanocomposites, is in accordance with the increase of the water permeability (Figure 5). The less exfoliated structure of the  $N_{32}^{100}\%$  film, composed of both individual clay layers and clay aggregates (Table 2 and Figure 2), could facilitate the penetration of water inside the nanocomposite and contribute to the rise of water permeation. To validate this interpretation, liquid water sorption measurements in nanocomposites were carried out. From the equilibrium state of the mass gain, the water concentration  $C_{eq}$  (g/g) has been determined by dividing the mass gain by the initial mass (dry state). As shown in Figure 6, the variation of  $C_{eq}$  with the C30B volume fraction is in good agreement with permeation data, showing an increase of the water concentration with increasing clay fraction, in particular for highly filled composites. Moreover, in a previous study,<sup>27</sup> to investigate the contribution of the modified nanoclays to water solubility, vapor water sorption measurements were performed on PA12 and Cloisite C30B, for different water activities and by means of a microbalance (DVS). It was found from the sorption isotherms that, despite the hydrophobic character of

**TABLE 6: Water Permeation Kinetic Coefficients of PA12/C30B Nanocomposites**

| films                            | $D_0$  | $\langle D \rangle$                            | $\gamma C_{eq}$ | $\gamma$                            | $C_{eq}$                  |
|----------------------------------|--|--|-----------------|-------------------------------------|---------------------------|
|                                  | ( $\text{cm}^2 \text{ s}^{-1}$ ) $\times 10^9$ | ( $\text{cm}^2 \text{ s}^{-1}$ ) $\times 10^9$ |                 | ( $\text{cm}^3 \text{ mmol}^{-1}$ ) | ( $\text{mmol cm}^{-3}$ ) |
| PA12                             | 1.53   | 3.62   | 1.52            | 2.16                                | 0.70                      |
| $N_{32}^{0.8\%}-N_{100}^{0.8\%}$ | 1.17–1.55                                      | 2.62–3.10                                      | 1.44–1.26       | 1.68–1.71                           | 0.85–0.73                 |
| $N_{32}^{1.3\%}-N_{100}^{1.3\%}$ | 0.97–1.18                                      | 3.15–2.88                                      | 2.02–1.54       | 3.16–2.26                           | 0.64–0.68                 |
| $N_{32}^{2.5\%}-N_{100}^{2.5\%}$ | 0.84–1.04                                      | 2.99–2.41                                      | 2.16–1.50       | 3.91–2.23                           | 0.55–0.67                 |
| $N_{32}^{4\%}-N_{100}^{4\%}$     | 1.19–0.83                                      | 2.73–2.21                                      | 1.50–1.71       | 1.89–2.44                           | 0.79–0.70                 |
| $N_{32}^{5\%}-N_{100}^{5\%}$     | 1.26–1.05                                      | 1.58–1.82                                      | 0.43–1.02       | 0.28–1.11                           | 1.54–0.91                 |



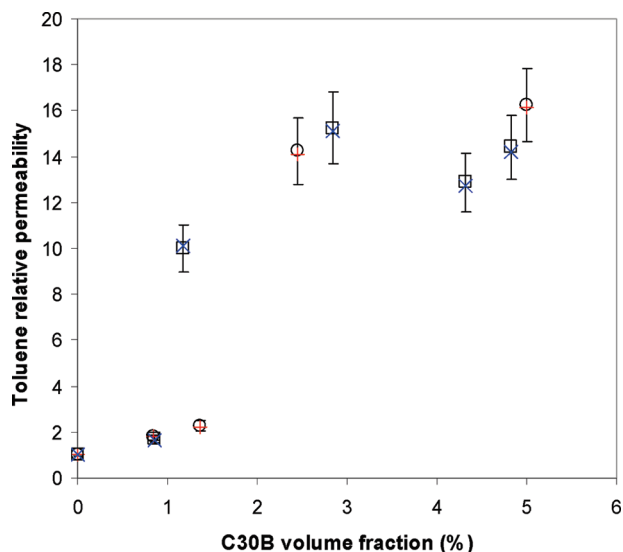


**Figure 7.** Toluene relative permeability as a function of montmorillonite mass fraction: (○) experimental results and (+) calculated values (eq 9) for N<sub>32</sub>% nanocomposites, (□) experimental results and (×) calculated values (eq 9) for N<sub>100</sub>% nanocomposites, respectively.

the organic part of C30B, the water solubility of C30B remained higher than that of PA12.

Finally, the permeation of water through the nanocomposite is much more complex than that of nitrogen. Indeed, water modifies the polymer/clay interface, and the solubility of water at the interface differs from the solubility in the bulk polymer. Water relative permeability calculated from eq 9, for N<sub>32</sub>% and N<sub>100</sub>% nanocomposites, is plotted in Figure 5. The very good agreement between experimental and calculated values confirms the relevance of the exponential law for the concentration-dependent diffusion coefficient. It is clear that the diffusivity depends not only on the tortuosity but also on the water concentration inside the nanocomposite films leading to the percolation effect.

**4.3.3. Toluene Permeability.** In contrast to water molecules, toluene molecules present a hydrophobic character. Therefore, the toluene molecule interactions with the PA12 matrix are different from the interactions with the clay/matrix interface. Contrary to permeation results with nitrogen and water, the presence of montmorillonite in the PA12 matrix increases the toluene permeability when the montmorillonite content increases (Table 5). The toluene relative permeability of nanocomposites is presented in Figure 7. For N<sub>32</sub>% and N<sub>100</sub>% nanocomposites, the toluene relative permeability very strongly increases with increasing C30B content (1 order of magnitude for high mass fractions). In comparison with water, it is rather difficult to show the influence of the exfoliation degree of the montmorillonite fillers on the toluene permeability, but it is clear that the hydrophilic/hydrophobic nature of the interface between the filler and the PA12 matrix plays an important role in the increase of the toluene permeation flux.

To explain such behavior, the toluene permeation kinetics were investigated. The experimental toluene flux curves were fitted with the exponential concentration-dependent diffusion law (eq 6). Except for the N<sub>32</sub>% nanocomposite film, which presents a constant diffusion coefficient, all composites present an excellent agreement between the experimental and calculated fluxes. The parameters of the concentration-dependent diffusion law are reported in Table 7. For all the samples studied, the toluene diffusion coefficients  $D_0$  and  $\langle D \rangle$  are 1 or 2 orders of magnitude lower than the water diffusion coefficients (Tables

6 and 7); indeed, the toluene molecule is bigger than the water molecule. Except for N<sub>32</sub>% and N<sub>32</sub>%, the nil toluene diffusion coefficient  $D_0$  is constant, irrespective of the mixing conditions. In fact,  $D_0$  depends mainly on the hydrophilic/hydrophobic character of the clay–polymer interface.

Following the method proposed by Herrera et al.,<sup>49</sup> the Flory–Huggins interaction parameter,  $\chi$ , estimating the interaction energy between the penetrant volatile organic compound species and the polymer segments, was calculated from eq 10 where  $a$  is the activity of the penetrant vapor phase;  $\phi_t$  is the

$$\ln a = \ln \phi_t + (1 - \phi_t) + \chi(1 - \phi_t)^2 \quad (10)$$

penetrant volume fraction (toluene); and  $\chi$  is the polymer–penetrant interaction parameter. In this study, the activity of the toluene was equal to 1 (liquid phase). The volume fraction of the toluene was determined from the mass gain at equilibrium state of sorption kinetics performed at 25 °C. The values of  $\chi$ , deduced from eq 10, were compared to the calculated values from eq 11<sup>50</sup>

$$\chi = \beta + \frac{V(\delta_t - \bar{\delta})^2}{RT} \quad (11)$$

where  $\beta$  is a constant equal to 0.34;  $V$  is the molar volume ( $V = 106.8 \text{ cm}^3/\text{mol}$  for toluene);  $\delta_t$  is the solubility parameter of toluene ( $18.1 \text{ (MPa)}^{1/2}$ ); and  $\bar{\delta}$  is the solubility parameter of polymer, modified by the presence of surfactant in clay.  $\bar{\delta}$  is defined as a linear combination of the solubility parameters of surfactant ( $=16.8 \text{ (MPa)}^{1/2}$ )<sup>51</sup> and PA12 ( $=20.45 \text{ (MPa)}^{1/2}$ ), weighted by clay and PA12 volume fractions.<sup>49</sup>

Interaction parameters  $\chi$  of nanocomposite/toluene systems, deduced from eq 10 or eq 11, are shown as a function of C30B volume fraction in Figure 8. The decrease of  $\chi$  with increasing clay fraction is the signature of a better miscibility between PA12 and C30B in the presence of toluene. The decrease of interaction parameter  $\chi$  is consistent with the fact that the surfactant aliphatic chain has a solubility parameter which is similar to toluene. As shown in Figure 8, both  $\chi$  interaction parameters seem to follow the same trend. The difference observed between the interaction parameters, deduced from eq 10 and eq 11, was discussed by Herrera et al.<sup>49</sup> it could be due to an oversimplistic model for the  $\chi$  interaction parameter of polar or slightly polar molecules, such as toluene, which have specific (directional) interactions. On the other hand, it is quite difficult to determine the solubility parameter of C30B because of the hydrophilic nature of the clay and the hydrophobicity of the ammonium surfactant.

The sorbed toluene molecules, like water molecules, increase the free volume during the permeation process. The toluene plasticization factor,  $\gamma C_{eq}$ , is twice as high as that for water and does not seem to be affected by the montmorillonite content [Table 7]. The plasticization phenomenon is more pronounced with organic vapors, such as toluene, than with water vapor.<sup>52</sup> The high  $\gamma$  level for the PA12 matrix, reported in Table 7, confirms the strong plasticization effect of toluene on the PA12, due to the strong interactions between toluene molecules and the hydrophobic PA12 chain segments. However, the plasticization coefficient  $\gamma$  is considerably reduced by the presence of montmorillonite in the PA12 matrix. For all composites, the strong  $\gamma$  drop results from a decrease of the free volume occupied by the toluene within the PA12 matrix. Moreover, the

TABLE 7: Toluene Permeation Kinetic Coefficients of PA12/C30B Nanocomposites

| films  | $D_0$<br>( $\text{cm}^2 \text{s}^{-1}$ ) $\times 10^9$ | $\langle D \rangle$<br>( $\text{cm}^2 \text{s}^{-1}$ ) $\times 10^9$ | $\gamma C_{\text{eq}}$ | $\gamma$<br>( $\text{cm}^3 \text{mmol}^{-1}$ ) | $C_{\text{eq}}$<br>( $\text{mmol cm}^{-3}$ ) |
|--|--|--|------------------------|--|--|
| PA12   | 0.039  | 0.33   | 3.39                   | 14.87  | 0.23   |
| $\text{N}_{32}^{0.8\%}-\text{N}_{100}^{0.8\%}$ | 0.039–0.037  | 0.40–0.50  | 3.65–4.01              | 10.85–15.92                                    | 0.34–0.25                                    |
| $\text{N}_{32}^{1.3\%}-\text{N}_{100}^{1.3\%}$ | 0.040–0.041  | 0.43–0.36  | 3.72–3.45              | 9.60–1.62                                      | 0.39–2.13                                    |
| $\text{N}_{32}^{2.5\%}-\text{N}_{100}^{2.5\%}$ | 0.040–0.037  | 0.52–0.37  | 3.95–3.60              | 1.92–1.16                                      | 2.06–3.10                                    |
| $\text{N}_{32}^{4\%}-\text{N}_{100}^{4\%}$     | 0.056–0.033  | 0.50–0.49  | 3.47–4.14              | 3.20–2.10                                      | 1.08–1.97                                    |
| $\text{N}_{32}^{5\%}-\text{N}_{100}^{5\%}$     | 0.034  | 0.3  | 3.75                   | 1.32   | 6.44–2.84                                    |

decrease of  $\gamma$  could be due to the reduction of the polymer chain segment flexibility due to the presence of clay entities<sup>44</sup> and to the presence of toluene, especially that located in the vicinity of the clay/PA12 interface. In that case, the sorbed toluene molecules would not contribute to the free volume variation. This was confirmed by the study of equilibrium toluene concentration  $C_{\text{eq}}$ :  $C_{\text{eq}}$  increases with montmorillonite content (Table 7). Moreover, it is interesting to note that the equilibrium toluene concentration variation is similar to the toluene relative permeability, revealing the strong influence of a thermodynamic contribution to the toluene permeability.

In short, the detailed analysis of the toluene permeation kinetics has highlighted the role played by the clay/matrix interface on the PA12/montmorillonite transport properties. Indeed, in the case of toluene, contrary to nitrogen and water molecules, the strong permeant/matrix interactions and the C30B/PA12 interface balance the tortuosity effect. The transport properties of nanocomposites are governed less by the increase of the diffusion path due to the presence of nanofillers and more by the interactions of diffusing molecules with fillers and matrix and by their diffusion, which is made easier in interfacial zones. The better compatibility between the hydrophobic matrix and the organo-modified montmorillonite improves the toluene diffusivity. Indeed, toluene molecules can get through the filled polymer film by going through the polymer but also by diffusing along a preferential path, lined with the clay/matrix interfacial zones. It is interesting to note that the toluene relative permeability was found to be higher for  $\text{N}_{100}^{x\%}$  than for  $\text{N}_{32}^{x\%}$  nanocomposites (Figure 6), which is consistent with the fact that the larger surface of the modified clay/matrix interface is obtained for the better exfoliated nanocomposites. Therefore, the toluene

relative permeability of nanocomposites cannot be determined from models based on a purely geometrical approach:<sup>11,14,34,35</sup> it is necessary to consider the concentration-dependent diffusion and the variation of solubility in modeling the permeability behavior. The toluene relative permeability value, calculated from eq 9, is plotted in Figure 7 for both types of nanocomposites. The excellent agreement between experimental and calculated toluene relative permeability value highlights the importance of the interactions between the diffusing species and (a) the matrix, (b) the nanofillers, and (c) the nanoclay/matrix interface.

## 5. Conclusion

To investigate the transport properties of the composites, three molecules, differing in their kinetic diameter and interaction capacity, were used.

Nitrogen, which presents very weak interactions with polymeric materials, was used to study the influence of montmorillonite structure on the transport properties of PA12/montmorillonite films. The geometrical model proposed by Nielsen and Bharadwaj was used to model the composite nitrogen permeability, which is governed by tortuosity effects. The fit confirms the slightly better exfoliation for the nanocomposites prepared at the highest blade rotation speed.

The influence of the clay/matrix interface on the transport properties of the composites was investigated by using two other molecules, water and toluene, interacting differently with the interfaces and the PA12 matrix.

The relative hydrophobic character of organo-modified C30B montmorillonite and the high tortuosity due to the nanostructure contribute to a decrease of water permeability at low C30B fractions. Beyond 4% volume fraction of C30B, the loss of barrier effect, especially for the less exfoliated nanocomposite, was attributed to the increase in the amount of sorbed water, leading to percolation paths of low diffusion resistance through the film.

Toluene permeability of nanocomposites is higher than that of the PA12 matrix, whatever the clay fractions. A higher plasticization effect of the composites was observed with toluene, compared to water. The long aliphatic chains of the surfactant lend a hydrophobic property to the clay and lead to an increase in the miscibility of the polymer/clay composite when exposed to toluene. The increase of the toluene permeability would thus result from the better compatibility between the hydrophobic matrix and the organo-modified montmorillonite. This compatibility enhances the toluene diffusivity: toluene molecules can get through the filled system by going through the polymer and also by diffusing along a preferential path, lined with clay/matrix interfacial zones, the surfactant aliphatic chain being characterized by a solubility parameter similar to that of toluene.

From the modeling point of view, we pointed out that a geometrical approach, which can be convenient for nitrogen

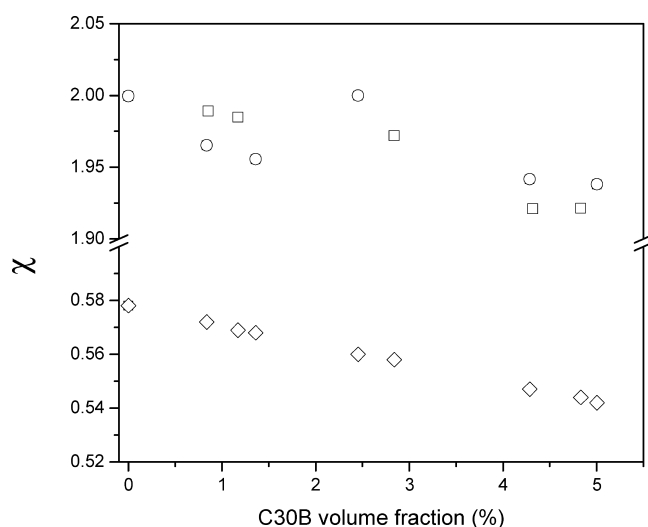


Figure 8. PA12/C30B–toluene interaction parameter, deduced from eq 10, at different C30B volume fraction: (○) for  $\text{N}_{100}^{x\%}$  nanocomposites, (□) for  $\text{N}_{32}^{x\%}$  nanocomposites. (◇) PA12/C30B–toluene interaction parameter, calculated from eq 11.

transport, is not sufficient to describe the transport of water and toluene through the PA12-based nanocomposite films. The analysis of the water and toluene permeation fluxes has shown that a concentration-dependent diffusion should be considered.

Finally, the barrier properties of nanocomposites were shown to depend on the degree of exfoliation of the clay particles but also on the interactions of diffusing molecules with the clay/matrix interface, leading to percolation paths.

**Acknowledgment.** RMPP “Réseau Matériaux Polymères Plasturgie” funding is gratefully acknowledged. Thanks to Dilys Moscato for her help in English.

## References and Notes

- (1) Yano, K.; Usuki, A.; Okada, A.; Kurauchi, T.; Kamigaito, O. *J. Polym. Sci., Part A: Polym. Chem.* **1993**, *31*, 2493–2498.
- (2) Lan, T.; Kaviratna, D.; Pinnavaia, J. *Chem. Mater.* **1994**, *6*, 573–575.
- (3) Osman, M. A.; Mittal, V.; Morbidelli, M.; Suter, U. W. *Macromolecules* **2003**, *36*, 9851–9858.
- (4) Takashi, S.; Goldberg, H. A.; Feeney, C. A.; Karim, D. P.; Farrell, M.; O’Leary, K.; Paul, D. R. *Polymer* **2006**, *47*, 3083–3093.
- (5) Ke, Z.; Youngping, B. *Mater. Lett.* **2005**, *59*, 3348–3351.
- (6) Gain, O.; Espuche, E.; Pollet, E.; Alexandre, M.; Dubois, P. *J. Polym. Sci., Part B: Polym. Phys.* **2005**, *43*, 205–214.
- (7) Picard, E.; Vermogen, A.; Gérard, J.-F.; Espuche, E. *J. Membr. Sci.* **2007**, *292*, 133–144.
- (8) Burnside, S. D.; Giannelis, E. P. *Chem. Mater.* **1995**, *7* (9), 1598–1600.
- (9) Xu, R.; Manias, E.; Snyder, A. J.; Runt, J. *Macromolecules* **2001**, *34*, 337–339.
- (10) Ogasawara, T.; Ishida, Y.; Ishikawa, T.; Aoki, T.; Ogura, T. *Composites, Part A* **2006**, *37*, 2236–2240.
- (11) Sun, L.; Boo, W.-J.; Clearfield, A.; Sue, H.-J.; Pham, H.-Q. *J. Membr. Sci.* **2008**, *318*, 129–136.
- (12) Drozdov, A. D.; Christiansen, J. D.; Gupta, R. K.; Shah, A. P. *J. Polym. Sci., Part B: Polym. Phys.* **2003**, *41* (5), 476–492.
- (13) Kim, J.-K.; Hu, C.; Woo, R. S. C.; Sham, M.-L. *Compos. Sci. Technol.* **2005**, *65*, 805–813.
- (14) Nielsen, L. E. *J. Macromol. Sci.* **1967**, *A1*, 929–942.
- (15) Bharadwaj, R. K. *Macromolecules* **2001**, *34*, 9189–9192.
- (16) Lan, T.; Kaviratna, P. D.; Pinnavaia, T. J. *Chem. Mater.* **1995**, *7*, 2144–2150.
- (17) Vaia, R. A.; Jandt, K. D.; Kramer, E. J.; Giannelis, E. P. *Chem. Mater.* **1996**, *8* (11), 2628–2635.
- (18) Vaia, R. A.; Giannelis, E. P. *Macromolecules* **1997**, *30*, 7990–7999.
- (19) Di, Y.; Iannace, S.; Di Maio, E.; Nicolais, L. *J. Polym. Sci., Part B: Polym. Phys.* **2003**, *41* (7), 670–678.
- (20) Fornes, T. D.; Paul, D. R. *Macromolecules* **2004**, *37*, 7698–7709.
- (21) Herrera-Alonso, J. M.; Maranda, E.; Little, J. C.; Cox, S. S. *J. Membr. Sci.* **2009**, *337*, 208–214.
- (22) Meng, X.; Wang, Z.; Zhao, Z.; Du, X.; Bi, W.; Tang, T. *Polymer* **2007**, *48*, 2508–2519.
- (23) Médéric, P.; Aubry, T.; Razafinimaro, T. *Int. Polym. Process.* **2009**, *3*, 261–266.
- (24) Dennis, H. R.; Hunter, D. L.; Chang, D.; Kim, S.; White, J. L.; Cho, J. W.; Paul, D. R. *Polymer* **2001**, *42*, 9513–9522.
- (25) Huang, X.; Lewis, S.; Brittain, W. J.; Vaia, R. A. *Macromolecules* **2000**, *33*, 2000–2004.
- (26) Xu, B.; Zheng, Q.; Song, Y.; Shangguan, Y. *Polymer* **2006**, *47*, 2904–2910.
- (27) Alexandre, B.; Langevin, D.; Médéric, P.; Aubry, T.; Couderc, H.; Nguyen, Q. T.; Saiter, A.; Marais, S. *J. Membr. Sci.* **2009**, *328*, 186–204.
- (28) Cho, J. W.; Paul, D. R. *Polymer* **2001**, *42*, 1083–1094.
- (29) Xenopoulos, A.; Wunderlich, B. *J. Polym. Sci., Part B: Polym. Phys.* **1990**, *28* (12), 2271–2290.
- (30) Lixon C., Ben Doudou B., Chappey C., Dargent E. Marais S. *J. Phys. Chem. B*, in press.
- (31) Dreux, F.; Marais, S.; Poncin-Epaillard, F.; Métayer, M.; Labbé, M.; Saiter, J. M. *Mater. Res. Innovations* **2003**, *7* (3), 183–190.
- (32) Métayer, M.; Labbé, M.; Marais, S.; Langevin, D.; Brainville, M.; Chappey, C.; Dreux, F.; Belliard, P. *Polym. Test.* **1999**, *18*, 533–549.
- (33) Dreux, F.; Marais, S.; Poncin-Epaillard, F.; Métayer, M.; Mabbé, M. *Langmuir* **2002**, *18*, 10411–10420.
- (34) Lape, N. K.; Nuxoll, E. E.; Cussler, E. L. *J. Membr. Sci.* **2004**, *236*, 29–37.
- (35) Gusev, A. A.; Lusti, H. R. *Adv. Mater.* **2001**, *13*, 1641–1643.
- (36) Marais, S.; Nguyen, Q. T.; Devallencourt, C.; Métayer, M.; Nguyen, U. T. T.; Schaezel, P. *J. Polym. Sci., Phys. Ed.* **2000**, *38*, 1998–2008.
- (37) Cohen, M. H.; Turnbull, D. *J. Chem. Phys.* **1959**, *31* (5), 1164–1169.
- (38) Prager, S.; Long, F. A. *J. Am. Chem. Soc.* **1951**, *73*, 4072–4075.
- (39) Fujita, H. *Fortschr. Hochpolym. Forsch.* **1961**, *3*, 1–47.
- (40) Frisch, H. L. *J. Polym. Sci.* **1957**, *61*, 93.
- (41) Marais, S.; Métayer, M.; Nguyen, Q. T.; Labbé, M.; Langevin, D. *Macromol. Theory Simul.* **2000**, *9* (4), 207–214.
- (42) Aubry, T.; Razafinimaro, T.; Médéric, P. *J. Rheol.* **2005**, *49*, 425–440.
- (43) Fornes, T. D.; Yoon, P. J.; Keskkula, H.; Paul, D. R. *Polymer* **2001**, *42*, 9929–9940.
- (44) Ait-Hocine, N.; Médéric, P.; Aubry, T. *Polym. Test.* **2008**, *27* (3), 330–339.
- (45) Vieth, W. R.; Sladek, K. J. *J. Colloid Sci.* **1965**, *20* (9), 1014–1033.
- (46) Xu, B.; Zheng, Q.; Song, Y.; Shangguan, Y. *Polymer* **2006**, *47*, 2904–2910.
- (47) Marais, S.; Métayer, M.; Labbé, M. *J. Appl. Polym. Sci.* **1999**, *74* (14), 3380–3395.
- (48) Marais, S.; Nguyen, Q. T.; Devallencourt, C.; Métayer, M.; Nguyen, U. T.; Schaezel, P. *J. Polym. Sci., Part B: Polym. Phys.* **2000**, *38* (15), 1998–2008.
- (49) Herrera-Alonso, J. M.; Maranda, E.; Little, J.; Cox, S. S. *Polymer* **2009**, *50*, 5744–5748.
- (50) Gulke, E. A. *Solubility parameter values: Polymer Handbook*, 4th ed.; Brandup, J.; Immergut, E. H., Grulke, E. A., Eds.; John Wiley & Sons, Inc.: New York, 1999.
- (51) Jang, B. N.; Wang, D.; Wilkie, C. A. *Macromolecules* **2005**, *38* (15), 6533–43.
- (52) Crank, J.; Park, G. S. *Diffusion in Polymers*; Academic Press Inc.: London and New York, 1968.